Monthly Notices
of the
ROYAL ASTRONOMICAL SOCIETY

MNRAS **452,** 289–300 (2015) doi:10.1093/mnras/stv1323

Star formation scales and efficiency in Galactic spiral arms

D. J. Eden,[1,2]★ T. J. T. Moore,[2] J. S. Urquhart,[3] D. Elia,[4] R. Plume,[5] A. J. Rigby[2] and M. A. Thompson[6]

[1]*Observatoire astronomique de Strasbourg, Université de Strasbourg, CNRS, UMR 7550, 11 rue de l'Université, F-67000 Strasbourg, France*
[2]*Astrophysics Research Institute, Liverpool John Moores University, IC2, Liverpool Science Park, 146 Brownlow Hill, Liverpool L3 5RF, UK*
[3]*Max-Planck-Institut für Radioastronomie, Auf dem Hügel 69, D-53121 Bonn, Germany*
[4]*Istituto di Astrofisica e Planetologia Spaziali – INAF, Via Fosso del Cavaliere 100, I-00133 Roma, Italy*
[5]*Department of Physics and Astronomy, University of Calgary, 2500 University Drive NW, Calgary, AB T2N 1N4, Canada*
[6]*Centre for Astrophysics Research, Science & Technology Research Institute, University of Hertfordshire, College Lane, Hatfield, Herts AL10 9AB, UK*

Accepted 2015 June 11. Received 2015 June 9; in original form 2014 November 14

ABSTRACT

We positionally match a sample of infrared-selected young stellar objects, identified by combining the *Spitzer* Galactic Legacy Infrared Mid-Plane Survey Extraordinaire, *Wide-field Infrared Survey Explorer* and *Herschel Space Observatory* Herschel infrared Galactic Plane Survey, to the dense clumps identified in the millimetre continuum by the Bolocam Galactic Plane Survey in two Galactic lines of sight centred towards $l = 30^\circ$ and 40°. We calculate the ratio of infrared luminosity, $L_{\rm IR}$, to the mass of the clump, $M_{\rm clump}$, in a variety of Galactic environments and find it to be somewhat enhanced in spiral arms compared to the interarm regions when averaged over kiloparsec scales. We find no compelling evidence that these changes are due to the mechanical influence of the spiral arm on the star formation efficiency rather than, e.g. different gradients in the star formation rate due to patchy or intermittent star formation, or local variations that are not averaged out due to small source samples. The largest variation in $L_{\rm IR}/M_{\rm clump}$ is found in individual clump values, which follow a lognormal distribution and have a range of over three orders of magnitude. This spread is intrinsic as no dependence of $L_{\rm IR}/M_{\rm clump}$ with $M_{\rm clump}$ was found. No difference was found in the luminosity distribution of sources in the arm and interarm samples and a strong linear correlation was found between $L_{\rm IR}$ and $M_{\rm clump}$.

Key words: stars: formation – Galaxy: structure – infrared: ISM – radio continuum: ISM.

1 INTRODUCTION

It is clear from many images of 'grand design' spiral galaxies that star formation and spiral arm topology are closely interlinked. However, the precise relationship between the physics of the spiral arms and the nature of their ensuing star formation is not yet clear. The influence on the spiral arms could either be that they are triggering one, or more, of the main evolutionary stages of star formation (Roberts 1969) or are organizing features for the star-forming material (Elmegreen & Elmegreen 1986; Vogel, Kulkarni & Scoville 1988). The main stages of star formation are represented by the conversion of atomic gas to molecular clouds, molecular clouds with internal dense clumps and the clumps forming cores from which the single stars form.

The evidence of the first of these potential influences is ambiguous. Increases in the efficiency of cloud formation from the neutral interstellar medium (ISM) have been both observed (Heyer & Terebey 1998) and predicted (Dobbs, Bonnell & Pringle 2006) but the results of Foyle et al. (2010) contradict this. They find no increase in that efficiency, or the star formation efficiency (SFE) in or out of the spiral arms of two spiral galaxies, NGC 628 and NGC 5194. There is also no observed difference in the fraction of the total molecular gas mass in the form of dense, star-forming clumps within clouds located in and out of spiral arms in the Milky Way, when averaged over kiloparsec scales (Eden et al. 2012, 2013). There are, however, large cloud-to-cloud variations in the dense-clump fraction. There are large increases in the star formation rate density ($\Sigma_{\rm SFR}$ in units of $\mathrm{M}_\odot\ \mathrm{yr}^{-1}\ \mathrm{kpc}^{-2}$) by factors of between ~ 3 and ~ 30 associated with spiral arms in the Galaxy. However, no more than 30 per cent of this results from increases in the integrated luminosity of the young stellar objects (YSOs) per unit molecular gas mass, while the rest is due to source crowding. Further, much of the residual increase in L/M can be ascribed to the inclusion of extreme star-forming complexes such as W49 and W51 in the samples (Moore et al. 2012).

This source crowding suggests that the dominant effect is due to the organizing nature of the spiral arms. However, Dobbs, Burkert & Pringle (2011) found that the spiral arms allow larger molecular clouds to form, by delaying clouds in their orbits, which may affect

★ E-mail: david.eden@astro.unistra.fr

the mass function of clusters that form within them (e.g. Weidner, Kroupa & Bonnell 2010). The star formation rate or efficiency in the higher column density clouds is not increased, however (Krumholz et al. 2010). The spiral arms may also be prolonging the lifetime of the clouds, lengthening the time-scale for star formation to occur, increasing the SFE. A study using the Galactic Ring Survey (Jackson et al. 2006) found that the clouds in the interarm regions dissipate quickly (Roman-Duval et al. 2009) with models also predicting this (Dobbs & Pringle 2013).

The aim of this study is to investigate the efficiency with which the dense clumps form stars and measure the variation of that efficiency from clump to clump and on kiloparsec scales, looking for changes associated with environment. To do this, it is necessary to use infrared (IR) wavelengths that trace the YSOs embedded within the clump. We therefore aim to combine IR surveys that trace the embedded stellar population of YSOs and the Bolocam Galactic Plane Survey (BGPS; Aguirre et al. 2011) to calculate the ratio of the IR luminosity to the clump mass, an analogue of the SFE, as a function of Galactocentric radius and Galactic environment. This stage of the hierarchical, evolutionary star-formation process (which converts atomic gas to molecular clouds to dense clumps to YSOs) is the last to be investigated. Our previous work has found factors of ∼2–3 increases in the ratio of YSO luminosity to molecular cloud mass, in clouds associated with spiral arms, but no enhancement in the average dense gas mass fraction (Eden et al. 2012, 2013; Moore et al. 2012). We would therefore expect to find similar factors of ∼2–3 increases in the average clump to YSO conversion efficiency, measured by $L_{\rm IR}/M_{\rm clump}$, on similar scales, although the results may be sample dependent in detail.

The two slices of the plane studied are the same as those outlined in Eden et al. (2012, 2013), the $l = 30^\circ$ region spanning $l = 28\overset{\circ}{.}50$–$31\overset{\circ}{.}50$ and the $l = 40^\circ$ region covering Galactic longitudes of $l = 37\overset{\circ}{.}83$–$42\overset{\circ}{.}50$. The $l = 30^\circ$ region extends to Galactic latitudes of $|b| \leq 1^\circ$, whereas the $l = 40^\circ$ region only covers latitudes of $|b| \leq 0\overset{\circ}{.}5$. The $l = 30^\circ$ region has three populations within it: foreground material which is possibly associated with the Sagittarius arm, the tangent region which is the tangent of the Scutum–Centaurus arm and the end of the long bar, which hosts the extreme star-forming region W43 (Nguyen Luong et al. 2011), and the background spiral arms, which are the Sagittarius and Perseus arms. The $l = 40^\circ$ region contains two passes of the Sagittarius arm, the outer edge of the Scutum–Centaurus tangent and the Perseus arm, as well as the interarm regions between the spiral arms.

A four-armed model of the spiral arm is assumed, as refined by multiple tracers, from H II regions (e.g. Georgelin & Georgelin 1976; Paladini, Davies & De Zotti 2004) to the H I distribution (Levine, Blitz & Heiles 2006) to combinations of tracers (e.g. Hou, Han & Shi 2009; Urquhart et al. 2013a,b). The four spiral arms are the Norma, Scutum–Centaurus, Sagittarius and Perseus arms.

In Section 2, we outline the data sets which are used for this project, with Section 3 detailing the reasoning behind the wavelength choices and the calculation of YSO luminosities, whilst in Section 4 we present the results and analysis and Section 5 is a discussion of the results. A summary and the concluding remarks follow in Section 6.

2 DATA SETS

2.1 IR data sets

The Galactic Legacy Infrared Mid-Plane Survey Extraordinaire (GLIMPSE) was a *Spitzer Space Telescope* Legacy Program, which (and with subsequent follow-ups) mapped two thirds of the Galactic plane as part of three separate surveys (Benjamin et al. 2003; Churchwell et al. 2009). The $l = 30^\circ$ and 40° regions fall in the section observed during GLIMPSE I, which covered the longitudes of $|l| = 10^\circ$–65°. The survey mapped this region at wavelengths of 3.6, 4.5, 5.8 and 8.0 μm using the Infrared Array Camera (Fazio et al. 2004) at spatial resolutions of <2 arcsec. The sensitivity limits at each wavelength were 15.5, 15.0, 13.0 and 13.0 mag, respectively, with the high reliability (≥99.5 per cent completeness) Point Source Catalogue containing ∼30 million sources (Churchwell et al. 2009).

The *Wide-field Infrared Survey Explorer* (*WISE*; Wright et al. 2010) mapped the whole sky at 3.4, 4.6, 12 and 22 μm with angular resolutions of 6.1, 6.4, 6.5 and 12 arcsec, respectively. 5σ point-source sensitivities of 0.08, 0.11, 1 and 6 mJy were achieved. A saturation limit of 330 Jy is found for the brightest sources at 22 μm, but this is considerably deeper than MSX at 21 μm, ∼2.7 Jy (Price et al. 2001; Lumsden et al. 2013).

Hi-GAL (Herschel infrared Galactic Plane Survey; Molinari et al. 2010a,b), a *Herschel Space Observatory* Open-time Key Project, has mapped the entire Galactic plane at 70, 160, 250, 350 and 500 μm at spatial resolutions of 4–40 arcsec using the PACS (Poglitsch et al. 2008) and SPIRE (Griffin et al. 2008) cameras. The 90 per cent completeness limits at each wavelength are 0.5, 4.1, 4.1, 3.2 and 2.5 Jy at the five wavelengths, respectively (Molinari et al. 2010b), for the $l = 30^\circ$ region.

A custom source extraction algorithm, CuTEx (Curvature Thresholding Extractor; Molinari et al. 2011), was designed to obtain source catalogues in each of the five Hi-GAL wavebands. `CuTEx` differentiates the image along four directions, *X*, *Y* and the two diagonals twice. Negatives found in the second differential image are taken to be sources as these are the peaks against the background as long as they are coincident with zeroes in the first differential image. A source is identified when it is above the threshold in all four differential directions. The identified sources are then fitted with 2D elliptical Gaussian profiles, centred at the positions above to extract the integrated fluxes.

These IR surveys and their extracted catalogues provide almost complete coverage of the mid-IR to the submillimetre wavelength range, covering the whole spectral energy distribution (SED) of embedded YSOs.

2.2 Bolocam Galactic Plane Survey

The BGPS mapped the two regions, $l = 30^\circ$ and 40°, as part of the 133 deg^2 northern Galactic Plane section of the survey ($l = -10\overset{\circ}{.}5$–$90\overset{\circ}{.}5$). The BGPS surveyed the continuum at 1.1 mm ($\nu = 271.1$ GHz), with an rms noise of 11–53 mJy beam^{-1} and an effective angular resolution of 33 arcsec.

Eden et al. (2012, 2013) derived distances, and as a result, masses and positions with respect to spiral arms or with Galactocentric radius to 989 catalogued sources (Rosolowsky et al. 2010), 793 and 196 for the $l = 30^\circ$ and 40° region, respectively. The masses found for the BGPS sources were predominantly in the range of masses associated with molecular clumps ($10^{1.5}$–10^3 M$_\odot$; Dunham et al. 2011), large, dense, bound regions within which stellar clusters and large systems form.

The 99 per cent completeness limits in the two fields are 450 and 550 M$_\odot$ at 14 kpc in the $l = 30^\circ$ and 40° regions, respectively (Rosolowsky et al. 2010).

3 SOURCE LUMINOSITY CALCULATIONS

3.1 IR wavelength choice

A YSO SED has two components (Molinari et al. 2008; Compiègne et al. 2010). The IR part of the SED comes from the embedded YSO (if already nuclear burning) and/or the accretion luminosity, while the larger cold envelope within which the YSO/H II region is embedded emits strongly at the submillimetre and millimetre wavelengths. The latter component may be physically independent of the star formation rate (SFR) or star-forming content of a given clump until the clump material begins to be cleared in the later evolutionary stages (Molinari et al. 2008; Urquhart et al. 2013b).

By fitting an SED to the Hi-GAL data, the suitability of including the longer IR and submillimetre wavelengths in a measurement of the YSO luminosity can be tested. These SEDs were fitted to the band-merged Hi-GAL sources that were positionally matched with the $l = 40^\circ$ BGPS sources. The $l = 40^\circ$ region was used as it has the lowest confusion levels of the two fields.

Before fitting a modified blackbody to the Hi-GAL SEDs, we scaled the SPIRE fluxes ($\geq$250 μm) by the ratio of the beam-deconvolved source size and beam size at the considered SPIRE wavelength (cf. Nguyen Luong et al. 2011). This corrects for the increase in the observed source size, and consequently the flux, at the longest *Herschel* wavelengths (e.g. Giannini et al. 2012), as well as for the larger beam size. The submillimetre fluxes are likely to be dominated by a cold envelope that is physically much larger than the embedded YSO. The longer wavelength sources also tend to contain multiple shorter wavelength detections within the larger beam.

The fitting strategy is that as described in Giannini et al. (2012), with the modified blackbody expressions and adapted constants the same as Elia et al. (2013). The free parameters are integrated flux, which is then converted to mass, M, and temperature, T, while the dust opacity exponent, β, is kept constant at 2. The fits do not include the 70 μm point as the greybody envelope may be contaminated by the emission of its protostellar content and this point generally lies above the fit.

The masses derived from the SED fits were compared to those calculated from BGPS data, both using a fixed temperature of 14 K (see fig. 3 of Eden et al. 2013) and with temperatures obtained from the SED fits. The result is shown in Fig. 1. The 1:1 ratio line is plotted over the distribution and it can be seen that the mass derived from the SED fitting is tracing the same mass as the 1.1-mm BGPS flux. This distribution also supports the use of a single temperature in the previous studies.

Since the two methods trace the same mass, it is safe to assume that the luminosity traced by the Hi-GAL data at wavelengths covered by the SED fit (160–500 μm) is dominated by the clump and the cold gas/envelope. This is not useful if trying to identify the clump-to-stars stage of the evolutionary sequence and measure its efficiency via L/M as M and L are not independent, and if they are calculated from the same data, M is essentially L/T. As a result, it is more pertinent to use shorter wavelength data, namely the 8 μm GLIMPSE data, 12 and 22 μm *WISE* data and the 70 μm Hi-GAL data. These will trace the luminosity produced by the accretion disc and the embedded YSO, i.e. the stellar component, and the calculated luminosity and mass will be relatively independent. The wavelengths shorter than 8 μm are not used as they contribute very little to the luminosity.

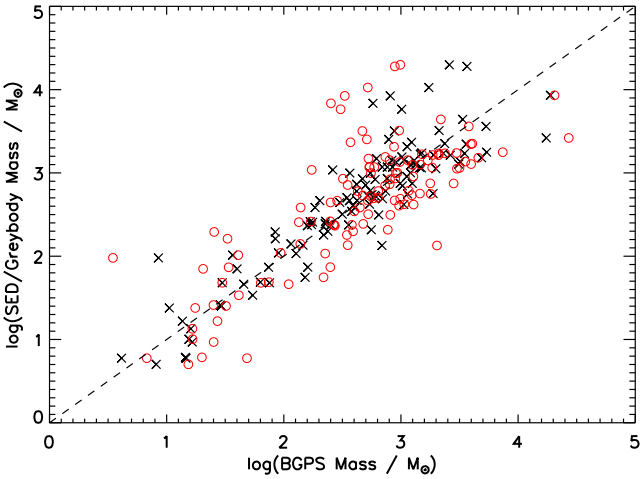

Figure 1. Comparison of SED-derived clump masses and masses calculated from the BGPS 1.1-mm flux density alone by Eden et al. (2013). The black crosses represent the BGPS masses calculated using the SED-derived temperature, whilst the red circles use a flat temperature of 14 K. The 1:1 line is indicated.

Table 1. Source counts at each wavelength in the $l = 30^\circ$ and 40° regions.

Survey	Wavelength	$l = 30^\circ$ Sources	$l = 40^\circ$ Sources
GLIMPSE	8 μm	204 367	163 848
WISE	12 and 22 μm	57 506	47 179
Hi-GAL	70 μm	4578	1469
BGPS	1.1 mm	806	229

3.2 Source associations

For a source to be considered a candidate YSO, it had to be catalogued in all four wavebands at 70 μm or shorter (i.e. 8, 12, 22 and 70 μm). The wavebands were combined by positional association. Starting at the largest beam size, an association in the waveband with the next largest was established if a source was found in that band within the beam radius. The order of the association was as follows: the *WISE* data at 6.5 and 12 arcsec for the 12 and 22 μm data, respectively (the *WISE* all-sky survey contains an already band-merged catalogue, so only sources with a flux, and an error on the flux, were used), the 70 μm Hi-GAL data with an aperture of 4 arcsec then the *Spitzer* GLIMPSE 8 μm with the smallest aperture of 1.9 arcsec. Table 1 gives the number of sources at each wavelength. The matching process resulted in multiple associations as data with smaller beam sizes were introduced. It is usually assumed that only one of the smaller-beam-size sources is the 'true' counterpart to the larger-beam-size components and the determination of the effect of an incorrect association where there is a choice is discussed in Section 3.4. A colour cut was applied that corresponded to the colour criteria used by the Red MSX Survey (RMS; Lumsden et al. 2013), which was $F_{22\,\mu\mathrm{m}} > F_{8\,\mu\mathrm{m}}$. This limits the sample to the embedded YSO stage similar to RMS, resulting in an IR selected sample of 1641 sources, 1050 and 591 in the $l = 30^\circ$ and 40° regions, respectively.

These associations were then positionally matched to the 1.1-mm BGPS sources, with only those sources that fell within the extent of

a BGPS source counted, as catalogued by Rosolowsky et al. (2010). This allows the distance of the BGPS source to be assigned to the IR source and only allow for IR sources to be counted which are part of a clump. These IR–BGPS associations resulted in a total of 241 IR sources in the $l = 30^\circ$ region and 107 in the $l = 40^\circ$ region with assigned distances.

In total, 298 BGPS clumps are associated with YSOs, 29 per cent of the total 1035 BGPS sources. Csengeri et al. (2014) found a 30 per cent association when matching ATLASGAL[1] and *WISE* sources. Of these 298 clumps, the vast majority are associated with a single IR source (250 or 84 per cent), with only two clumps found to be associated with three IR sources, one in each of the two regions.

To estimate the number of chance alignments, a Monte Carlo simulation was conducted, in which 1641 sources were distributed over the $l = 30^\circ$ and 40° regions. The random distribution of simulated sources accounted for the true clustering scales of the IR sources by maintaining the relative position of sources found within a BGPS beam of each other. These sources were then matched with the BGPS source catalogue. Hundred repeats found that the percentage of sources aligned with BGPS detections had a mean value of 0.8 ± 0.3 per cent, compared to the actual association alignments of 14.7 per cent.

3.3 Galactocentric radius distributions

Using the assigned velocities and distances from Eden et al. (2012, 2013) for the BGPS clumps, and hence the YSOs, the distribution of the clumps and YSOs as a function of Galactocentric radius can be produced. These are displayed in the upper panel of Fig. 2. The ratio of these distributions is presented in the lower panel. This quantity gives the number of YSOs per dense clump and can be used as an analogue of the SFE. The absolute luminosity-to-mass ratio as a function of Galactocentric radius is presented in Fig. 7 and discussed in Section 4.3. The peaks in both distributions occur at the positions of the Scutum–Centaurus tangent and W43. This is not surprising considering that the line of sight is down the spiral arm and W43 is the most prominent star-forming region in either of the lines of sight.

The number count ratio is relatively flat across most Galactocentric radii, with almost all the values for each 0.5 kpc bin falling within 1σ or 2σ of the mean. The mean value is found to be 0.46 with a standard deviation of 0.20 and a standard error on the mean of 0.07. The exceptions, however, are the bins at Galactocentric radii of 4–5 kpc, with values $\sim 5\sigma$ below the mean. These radii are associated with the Scutum–Centaurus tangent as well as the W43 star-forming region. Motte, Schilke & Lis (2003) and Nguyen Luong et al. (2011) interpret this as evidence that the SFR will be higher in the future in W43 due to an excess of starless clumps.

3.4 Luminosity calculations and the effect of incorrect association

Two methods were used to calculate the YSO luminosities: an integration using the trapezium rule method and the online SED fitting tool of Robitaille et al. (2007). The latter makes use of a library of 200 000 models of YSOs. A detailed description of the models can be found in Robitaille et al. (2006, 2007). The trapezium integration assumes no physical model but may underestimate the total luminosity as there is no correction for the missing wavebands or contributions to the IR flux from the cold envelope component. The SED fits are based on models that may not be appropriate but provide the above extrapolation based on a spectral shape that is generally plausible.

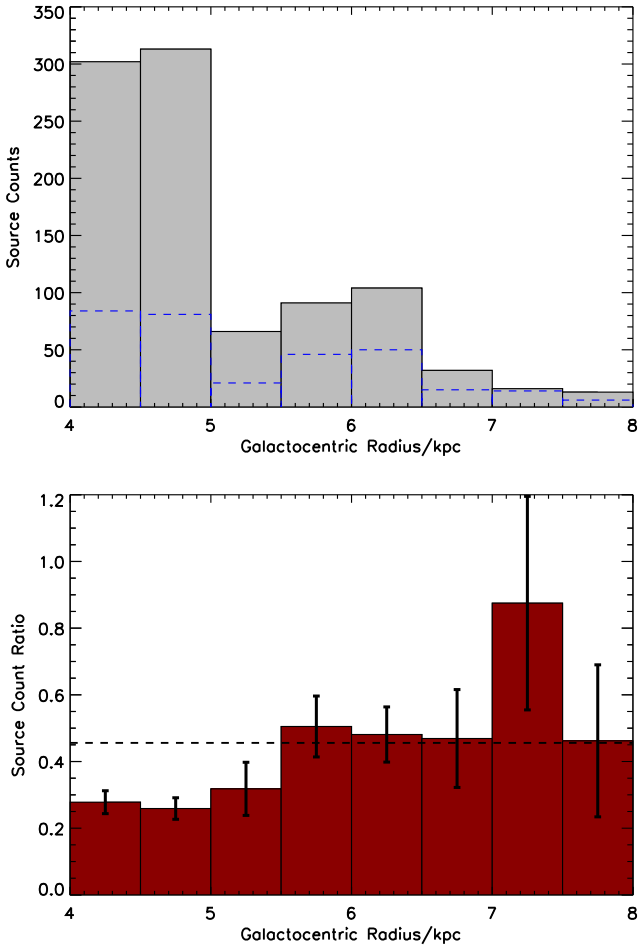

Figure 2. Upper panel: Galactocentric radius distribution of the BGPS clumps (grey filled histogram) overlaid with the YSOs (blue-dotted histogram). Lower panel: ratio of the two distributions, with the mean value of 0.46 indicated by the dashed line. The errors are derived using Poissonian statistics.

The distribution of the Robitaille SED calculated luminosities compared to the trapezium rule luminosities is shown in Fig. 3. The comparison shows the 50 per cent limits of the distribution of L value ratios and 63 per cent of sources are found within these limits. The distribution is skewed to excess luminosity in the model SEDs. As can be seen from the right-hand panel of Fig. 4, SEDs fitted to these sources tend to have a significant component of emission at near-IR, or submillimetre, wavelengths, where we have no data constraints. This is symptomatic of the sources with an SED fit which overestimates the IR luminosity, a large component from either the submillimetre or near-IR. The sources with a greater trapezium integration are overluminous at 70 μm. This makes the Robitaille fits unsuitable for those purposes as we are attempting to determine the IR luminosity independent of the submillimetre clump component. Fig. 4 shows an example SED fit with a consistent trapezium-rule luminosity and one with a significantly overestimated Robitaille luminosity.

[1] APEX Telescope Large Area Survey of the Galaxy.

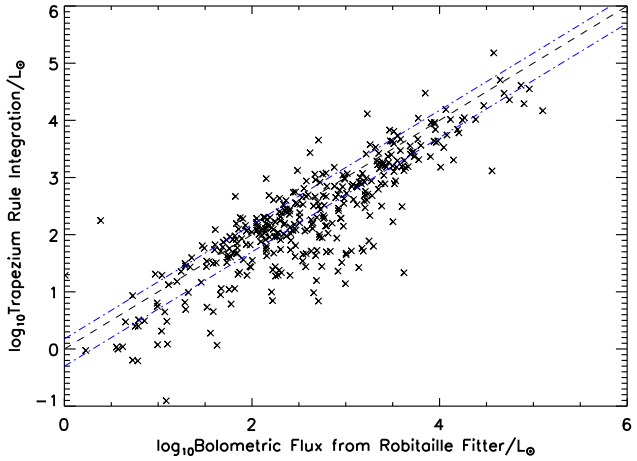

Figure 3. The comparison of IR-BGPS sources showing the correlation between the trapezium-rule integration and the Robitaille model luminosity. The 1:1 line is shown as the dashed line whilst the 50 per cent limits are the blue dot–dashed lines.

As a result, the luminosities of the YSOs used for this study were estimated via the trapezium rule. This however introduced a potential systematic error to the calculations since any emission at wavelengths <8 μm or >70 μm is not accounted for. However, the absolute values of the luminosity are less important than the comparative values and such biases are assumed to be similar across the sample. Veneziani et al. (2013) estimated bolometric luminosities, rather than IR luminosity, via a similar method to the trapezium rule, using those luminosities to produce SFRs and L–$M_{\rm clump}$ relations for the two Hi-GAL science demonstration fields.

As mentioned above, multiple GLIMPSE and Hi-GAL sources were often found to be associated with a single *WISE* source, or vice versa, due to the different spatial resolutions. We therefore investigated the effect of making an incorrect choice of multiple components on the final calculated luminosity.

By fitting SEDs to all the potential IR source matches for a given BGPS source in a subset of the sample, we investigated the uncertainty in luminosity values from the choice of source. Although some match combinations produced drastically better fits than others, the resulting luminosities were found to vary by less than 10 per cent. It is therefore clear that, for these purposes, there is no need to be overly concerned with identifying the correct counterpart and that the luminosity is dominated by wavebands (22 and 70 μm) in which there are few or no choices. Use of the trapezium rule produced similar results, with luminosities from each potential set of matches that were consistent within the measurement uncertainties. However, the absolute luminosities produced by the two methods were different.

4 RESULTS AND ANALYSIS

4.1 Star formation efficiencies

The star formation efficiency, or SFE, considered here, one of several analogous variants, is the fraction of dense, dust-continuum-traced clump material that has been converted into stars over some time-scale. As with the clump formation efficiency (CFE; the ratio of clump mass to cloud mass) analysis in Eden et al. (2012, 2013), the SFE within the separate populations of clumps along the two lines of sight can be estimated. The SFE is the ratio of the luminosity produced by embedded young stellar objects to the mass of the clumps.

The ratio of IR luminosity of YSOs to clump mass is a measure of

$$\frac{L_{\rm star}}{M_{\rm clump}} = \frac{1}{M_{\rm clump}} \int_0^t \frac{{\rm d}L}{{\rm d}t}\,{\rm d}t, \qquad (1)$$

where ${\rm d}L/{\rm d}t$ is the instantaneous SFR in terms of L. A high value for L/M can indicate either a high SFR or a longer time-scale. Equating L/M with the SFE therefore requires a few assumptions. For precise linear dependence, ${\rm d}L/{\rm d}t$ must be proportional to ${\rm d}M/{\rm d}t$ which requires that the stellar IMF is fully sampled in all star-forming regions, up to the maximum stellar masses, i.e. 'sorted sampling' filling the IMF (Weidner & Kroupa 2006). If, as seems likely, this is not the case and the IMF is filled stochastically (Elmegreen 2006),

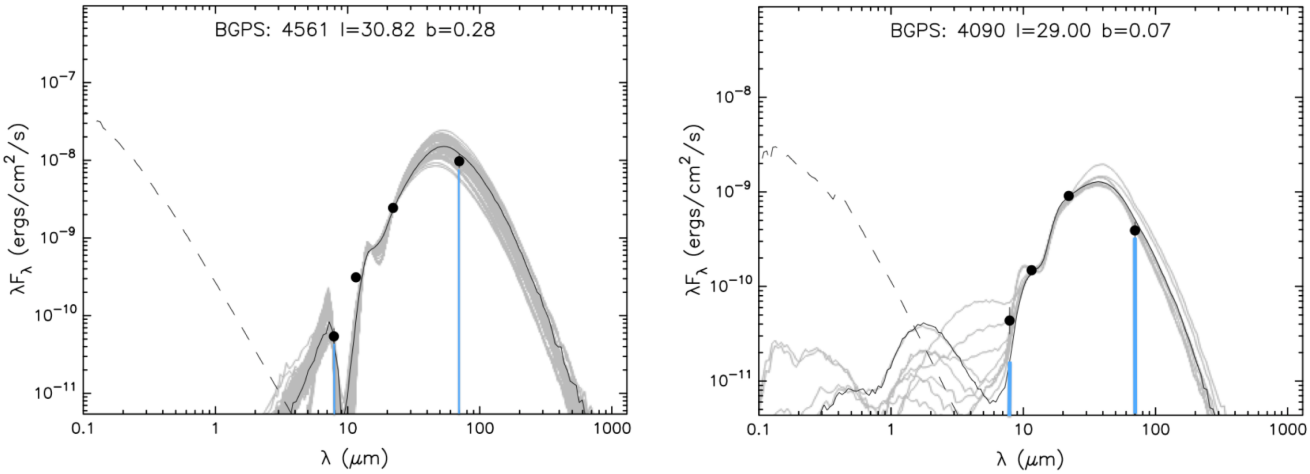

Figure 4. Example Robitaille SEDs with the trapezium-rule integration limits marked by the two blue lines. The SED-fit luminosity is the total area under the curve. The black points are the data points to calculate the best fit, and the black line represents the best fit with the next best nine fits represented in grey. The dashed line shows the best model if a stellar object is assumed with no circumstellar extinction. Left-hand panel: a source which exhibits similar luminosities for the Robitaille and trapezium-rule fits is shown with a trapezium-rule luminosity of 1.4×10^4 L$_\odot$ and Robitaille-fit luminosity of 2.4×10^4 L$_\odot$. Right-hand panel: a source which exhibits an extreme difference in luminosity between the Robitaille and trapezium-rule fits is shown with a trapezium-rule luminosity of 3.1×10^2 L$_\odot$ and Robitaille-fit luminosity of 4.0×10^3 L$_\odot$.

Table 2. SFEs calculated from the YSO luminosity to clump mass ratio for the populations within the $l = 30^\circ$ and 40° regions.

Region	Population	$L_{\rm IR}$ ($L_\odot$)	No. of YSOs	$M_{\rm clump}$ ($M_\odot$)	No. of clumps	SFE ($L_\odot/M_\odot$)
	Foreground	6750 ± 193	28	10300 ± 648	72	0.65 ± 0.05
$l = 30^\circ$	Tangent	523 000 ± 5090	160	544 000 ± 9990	615	0.96 ± 0.02
	Background	492 000 ± 6270	53	144 000 ± 6880	106	2.47 ± 0.09
$l = 40^\circ$	Total arm	191 000 ± 2570	77	137 000 ± 9180	135	1.40 ± 0.10
	Total interarm	59 700 ± 2880	30	83 300 ± 7070	61	0.72 ± 0.07

then L/M still has a direct dependence on the SFE but it may be non-linear. Then, an increase in SFE must produce an increase in L/M but an observed increase in L/M can also be the result of the formation of a larger cluster at the same efficiency ($L \propto M^2$ for clusters). Such an increase in L/M cannot be accounted for observationally until it is possible to count all the individual stars within a cluster. Another source of non-linearity may be introduced if the SFE is high, in which case, $M_{\rm clump}$ is no longer constant, but SFE values appear to be generally less than 30 per cent (e.g. Lada & Lada 2003; Johnston et al. 2009) and so $M_{\rm clump}$ is taken to be constant over the lifetime of a star-forming event as traced by mid- and far-IR detections. In principle, L/M also increases with time and the SFE is usually defined with respect to some characteristic time-scale; however, the stage of massive star formation traced by mid-IR emission is short (less than a few $\times\ 10^5$ yr: Davies et al. 2011; Mottram et al. 2011b) and our L/M determination can be taken as a snapshot of the current SFE. Variations in L/M can also be used as potential evolution indicators (Molinari et al. 2008; Urquhart et al. 2014b) although L and $M_{\rm clump}$ tend to show a linear relationship with little evidence of evolution in L/M during the IR-bright phase (Urquhart et al. 2014b).

The clump populations can be divided into those belonging to the foreground spiral arms, the tangent region consisting of the Scutum–Centaurus tangent and the end of the long bar, and the background Sagittarius and Perseus arms in the $l = 30^\circ$ region and the spiral arm and interarm regions in $l = 40^\circ$. The $l = 30^\circ$ region populations were separated using the distribution of the distances to the molecular clouds from Roman-Duval et al. (2009), as outlined in Eden et al. (2012). Eden et al. (2013) details how the molecular clouds, and hence, the BGPS clumps were assigned to spiral arm and interarm populations in the $l = 40^\circ$ region using the Galactic rotation model of Vallee (1995).

Using the masses derived for the BGPS sources by Eden et al. (2012, 2013) and IR luminosities for the associated YSOs obtained using the trapezium-rule integrations, we calculate the integrated luminosity and clump mass in each of the populations in the $l = 30^\circ$ and 40° fields and use the ratio, L/M as an estimate of the SFE averaged over the scale of the field. The values for each region are displayed in Table 2. BGPS-traced clumps are included whether or not they contain IR sources since they contribute to the total L/M.

The results for the $l = 30^\circ$ region differ from the results that are found in Eden et al. (2012) who found consistent CFEs in the tangent and background region and an increase in the foreground. The SFEs for each region depart from each other by factors of $\sim$2, that are significant within errors. The $l = 40^\circ$ region shows that arm population has a value twice that of the interarm. The implications of this are discussed in Section 5.1.

The uncertainties on the SFEs are a combination of the uncertainties in BGPS flux densities (Rosolowsky et al. 2010), the variance of the temperature distribution of the source populations, the catalogued flux uncertainties on the GLIMPSE and *WISE* sources (Churchwell et al. 2009; Wright et al. 2010), as well as the recently released Hi-GAL catalogues (Molinari et al., in preparation) containing the source flux uncertainties.

In summary, the average SFEs for the spiral arms are enhanced compared to the interarm regions by a factor of $\sim$2. However, there is a suppression towards the W43 star-forming region back to the interarm level. The other spiral arms, especially the Perseus arm, show an elevated SFE.

4.2 Luminosity functions

The luminosities of the YSOs were used to plot the luminosity functions (LFs) of the Scutum–Centaurus tangent region and of the other spiral arm regions. The spiral-arm subsample includes all YSOs found in the background region of $l = 30^\circ$ and the Perseus and Sagittarius YSOs from $l = 40^\circ$ as the background region consists of Sagittarius and Perseus YSOs. All sources with a heliocentric distance of less than 2 kpc are omitted, in order to remove local sources that may contaminate the results and avoid including a large number of low-luminosity YSOs below the completeness limit at Galactocentric radii of 8 kpc. No interarm LF is made due to the lack of sources.

The LFs of these two populations are presented in Fig. 5. The plotted quantity, $\Delta N/\Delta L$, is the number of sources per unit luminosity interval in each luminosity bin, with the luminosity point representing the median value of the bin. A fixed number of sources per bin was used, as opposed to fixed bin widths, in order to equalize weights determined from Poisson errors.

If it is assumed that the data in both populations are distributed as a power law of the form $\Delta N/\Delta L \propto L^\alpha$, a least-squares fit to each LF gives indices of $\alpha = -1.55 \pm 0.05$ and $\alpha = -1.57 \pm 0.07$ for the tangent and arm regions, respectively. Both LFs begin to flatten at luminosities $\sim\log(L/L_\odot) = 2.5$ which we assume to indicate the sample completeness limit. The index values for these populations are consistent with each other, which shows that, in terms of the resulting distribution of YSO luminosities, the star-formation process at the end of the bar is no different to that in other spiral arms, despite the inclusion of the W43 region.

These slopes are consistent with that of the RMS survey (Lumsden et al. 2013). Plotting the luminosities of both YSOs and H II regions (Mottram et al. 2011a; Urquhart et al. 2014a) with equal population bins gives indices of $\alpha = -1.48 \pm 0.04$ and $\alpha = -1.60 \pm 0.04$ for the YSO and H II populations, respectively. A combined sample had an index of $\alpha = -1.50 \pm 0.02$.

Further evidence for the similarity of the star formation in the two populations is that a Kolomogorov–Smirnov (K–S) test shows a 27 per cent probability that they are drawn from the same population, which is only a 1σ departure. Thus, we are unable to reject the

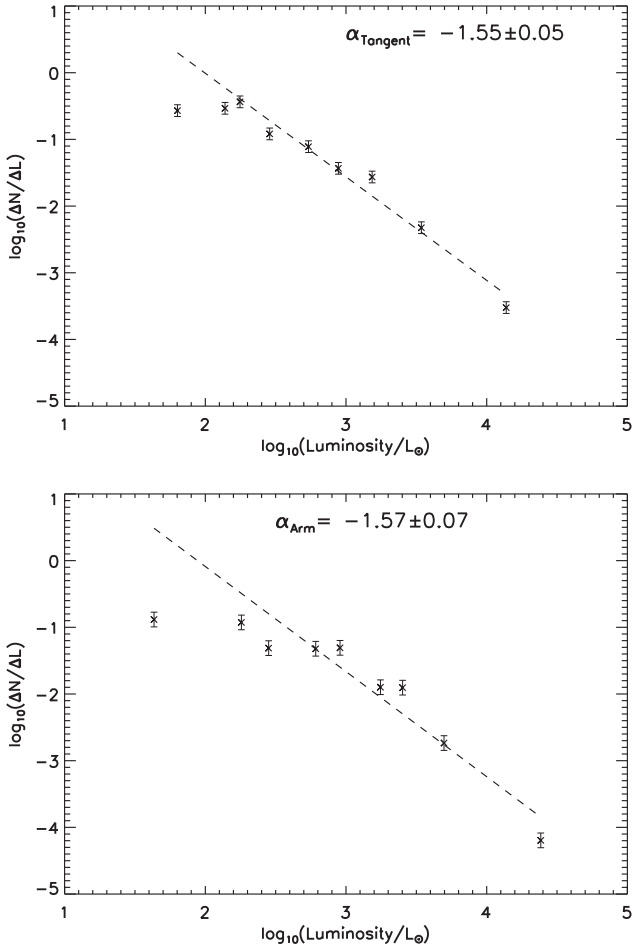

Figure 5. LFs for the Scutum–Centaurus tangent region and all other spiral arm regions. The dashed lines are fits to the slope of the LF. The error bars correspond to $\sqrt{N}$ counting statistics. Top panel: Scutum–Centaurus region. Bottom panel: spiral arm regions with sources of heliocentric distances less than 2 kpc omitted from both the $l = 30^\circ$ and 40° regions.

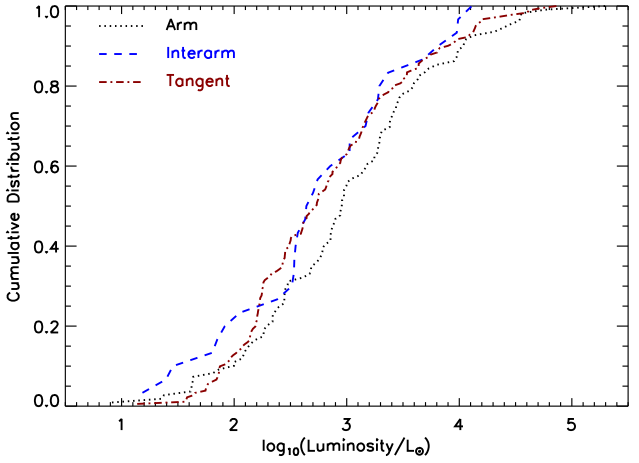

Figure 6. The cumulative distribution function of the spiral arm, interarm and tangent region samples. The spiral arm sample is represented by the black-dotted line, the interarm sample by the blue-dashed line and the tangent by the red dot–dashed line. The spiral arm sample again has sources of heliocentric distances less than 2 kpc omitted.

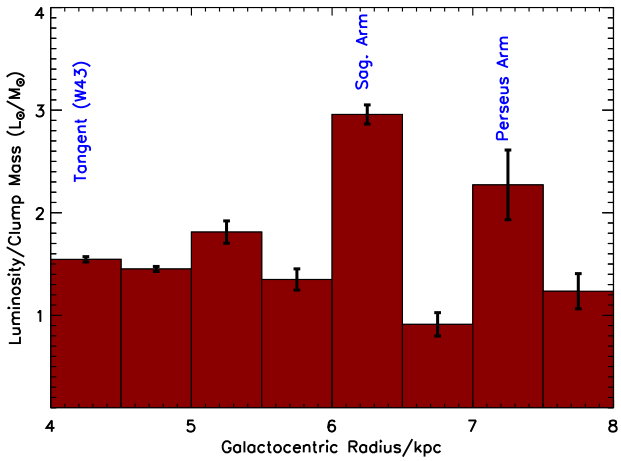

Figure 7. The total L/M as a function of Galactocentric radius within the studied regions centred at $l = 30^\circ$ and 40°. The Galactocentric radii associated with spiral arms are labelled. Sources with heliocentric distances less than 2 kpc are omitted, to remove local sources at Galactocentric radii of ∼8 kpc.

null hypothesis that they are drawn from the same population. Even though no LF was produced for the interarm regions, by performing a K–S test with the interarm sources, it showed a 23 per cent probability that they are drawn from the same population so there is no evidence for a variation in the current data. The cumulative distributions of the three samples are displayed in Fig. 6, and the similarity of the three distributions reflects the K–S test results. It is worth noting that the interarm sample is very small and not a strong constraint on the nature of interarm star formation.

4.3 L/M distribution with Galactocentric radius

The distribution of L/M as a function of Galactocentric radius is displayed in Fig. 7. All sources with heliocentric distances under 2 kpc are again omitted. A significant peak is found at 6 – 6.5 kpc, with an increase by factors of 2.2 and 3.2 over the adjacent bins, which correspond to 7.8σ and 9.3σ peaks, respectively. A less pronounced peak is found at 7–7.5 kpc, with 4.1σ and 3.1σ departures found compared to adjacent bins, which are increases in factors of 2.5 and 1.9, respectively. The first peak corresponds to the Sagittarius spiral arm, whilst the second is the Perseus spiral arm.

Moore et al. (2012) found peaks associated with the Sagittarius and Perseus arms in the $L/M_{\rm cloud}$ distribution, using the CO-traced molecular cloud mass. These peaks were found to be extreme in their study due to the presence of the star-forming regions W51 and W49A, respectively. However, when they removed these star-forming regions, the Perseus arm had a SFE similar to the levels in the adjacent bins whereas the removal of W51 from the Sagittarius arm reduced the peak relative to the neighbouring bins but the peak remained.

This study has neither the W49 or W51 star-forming regions within the two lines of sight investigated. As a result, the distribution as seen in Fig. 7 should reflect that of Moore et al. (2012), once those regions are omitted as the $M_{\rm clump}/M_{\rm cloud}$ ratio is constant (∼5–10 per cent) over large scales (Eden et al. 2012, 2013). The peak associated with the Sagittarius spiral arm is still elevated compared to the adjacent bins, whereas the Perseus arm bin at 7 kpc has a marginal peak compared to the bins either side, hence reflecting the Moore et al. (2012) distribution.

No peak is found at 4 kpc, the radius associated with the Scutum–Centaurus tangent and the extreme star-forming region, W43,

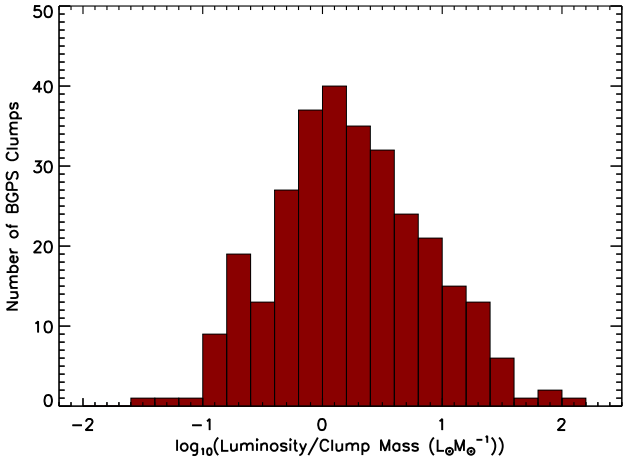

Figure 8. The ratio of YSO luminosity to BGPS clump mass for all clumps with at least one associated YSO in the $l = 30^\circ$ and 40° regions. The bin size is 0.2 dex.

suggesting that the current star formation in W43 is unspectacular in terms of the YSO luminosity being produced per unit gas mass.

4.4 L/M ratios of individual clumps

The L/M ratio of individual BGPS clumps can be calculated and the distribution of these values ranges from 0 to 140 $L_\odot/M_\odot$. The mean value is 5.24 ± 0.70 $L_\odot/M_\odot$ with a median of 1.72 ± 1.14 $L_\odot/M_\odot$.

The distributions of L/M values in the separate regions listed in Table 2 are statistically indistinguishable and can be assumed to be a single population. We can therefore combine these samples and the distribution of the total L/M ratios for individual clumps is shown in Fig. 8. The total distribution, as with the CFEs in Eden et al. (2012, 2013), can be considered a lognormal distribution as Anderson–Darling and Shapiro–Wilk normality tests gave probabilities of 0.434 and 0.563, respectively, that the distribution is lognormal. The presence of a lognormal distribution indicates that the variation in L/M is likely to be due to the random variations in a collection of individual processes that multiply together to produce the observed values, and this suggests that those values in the wings of the distribution both with low and high L/M are not the result of fundamentally different processes. No correlation of L/M with clump mass was found. Therefore, the spread of values in Fig. 8 is intrinsic and the result of natural variations in the star-formation process within clumps that are independent of this basic property.

The lognormal distribution can be fitted with a Gaussian that has a mean of 0.08 and a standard deviation of 0.57 dex. With these parameters, three clumps can be found to have IR luminosity-clump mass ratios that are greater than the mean by more than 3σ. With the probabilities of these events, only one source at these significances would be expected in a sample of this size. These three clumps are all found in the Scutum–Centaurus tangent in the $l = 30^\circ$ region. These clumps have BGPS IDs of 4497, 4561and 4617 with masses of 104, 197 and 97 $M_\odot$, respectively. These all have one associated YSO which have luminosities of $\log(L/L_\odot) = 3.94$, 4.15 and 4.13.

The absolute SFE values ($M_{\rm star}/M_{\rm clump}$) can be calculated for all the clumps which have an associated luminosity of $\log(L/L_\odot) > 3.01$ by using the stellar luminosities outlined in Mottram et al. (2011b) for spectral types B3 and greater, calculated by using a 1 Myr isochrone to local OB stellar populations using the stellar rotation models of Meynet & Maeder (2003). The range of these SFEs is from 0.1 to 14.3 per cent with a mean value of 1.9 ± 0.3 per cent and a median of 0.9 per cent, consistent with those of Smith (2014). As these are most likely to be the sites of cluster formation, the SFEs calculated here are lower limits. This is only the SFE derived from the brightest source and likely missing most of the lower mass YSOs.

As we have determined the L/M ratios of the individual clumps that contain a YSO, the range can be compared to those found for molecular clouds and whole spiral arms, to determine the scale at which the most drastic variations are occurring. The range of $L/M_{\rm clump}$ for the individual clumps that have a YSO is 0.04 ± 0.01–140 ± 22 $L_\odot/M_\odot$. The range of $L/M_{\rm cloud}$ is 0.02 ± 0.01–68 ± 13 $L_\odot/M_\odot$ and $L/M_{\rm arm}$ is 1.00 ± 0.02–2.9 ± 0.2 $L_\odot/M_\odot$.

5 DISCUSSION

5.1 Star formation on kiloparsec scales

Eden et al. (2012, 2013) found that the dense-clump mass fraction in clouds ($M_{\rm clump}/M_{\rm cloud}$) varies by more than three orders of magnitude from cloud to cloud ($\sigma = 0.57$) on spatial scales of 10–100 pc. However, on kpc scales and between arm and interarm components, $M_{\rm clump}/M_{\rm cloud}$ is consistent with being constant, within the current uncertainties, and is seemingly unaffected by the presence of a spiral arm. Moore et al. (2012) showed that $L/M_{\rm cloud}$, averaged over kpc scales, increases a little in some spiral arms, relative to the nearby interarm regions, but not in others. In particular, the Scutum–Centaurus arm tangent shows no increase in $L/M_{\rm cloud}$, despite being the location of a large enhancement in the surface density of the star formation rate ($\Sigma_{\rm SFR}$). Most of the large increases in $\Sigma_{\rm SFR}$ associated with spiral arms are therefore due to crowding, rather than a change in the star-forming capacity of clouds. The residual enhancements in $L/M_{\rm cloud}$ that were found in other arms are largely due to the inclusion of extreme star-forming regions such as W49A and W51 in the samples examined.

From the current work (Fig. 7), we see that there are also increases in $L/M_{\rm clump}$ associated at least with the Sagittarius arm, and possibly also with the Perseus arm, by factors of about 2, compared to the interarm regions, but, again, no enhancement in the Scutum–Centaurus tangent. Since we have evidence that $M_{\rm clump}/M_{\rm cloud}$ is constant on these scales, we expect that any variations in $L/M_{\rm clump}$ in the present study would be consistent with those found in $L/M_{\rm cloud}$ by Moore et al. (2012) and, allowing for the differences in the samples used in the two studies (the current study does not include W49A, for example), this is indeed what we find.

The enhancements by a factor of $\sim$2 in the average $L/M_{\rm clump}$ found in some spiral arms (Sagittarius and Perseus) but not in others (Scutum–Centaurus) might be explained by different time gradients in the SFR in different places. If we remove the apparently non-star-forming clumps from the calculation of $L/M_{\rm clump}$ (i.e. those clumps without an IR source), we find that a $\sim$30 per cent enhancement appears at the radius of the Scutum–Centaurus tangent (Fig. 9) with respect to the adjacent radii. $L/M_{\rm clump}$ here is larger by a factor of $\sim$3 than the value obtained when the starless clumps are included in $M_{\rm clump}$. Elsewhere within a radius of $\sim$6.5 kpc, $L/M_{\rm clump}$ increases by a factor closer to 2 than when starless clumps are not counted. This is consistent with the idea that the Scutum–Centaurus tangent region has a larger-than-average reservoir of dense clumps yet to form stars. Nguyen Luong et al. (2011) predict that the SFR in clouds associated with the W43 star-forming region, which is within the tangent and included in our sample, will be five times greater in the future than the current rate. Beyond 6.5 kpc, and including the

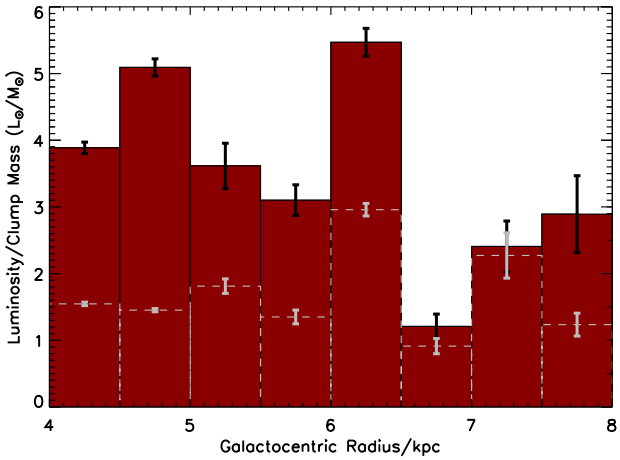

Figure 9. The L/M as a function of Galactocentric radius within the studied regions centred at $l = 30^\circ$ and 40° with the non-star-forming clumps removed. The distribution from Fig. 7 is shown by the grey, dashed line. Sources with heliocentric distances less than 2 kpc are omitted, to remove local sources at Galactocentric radii of ∼8 kpc.

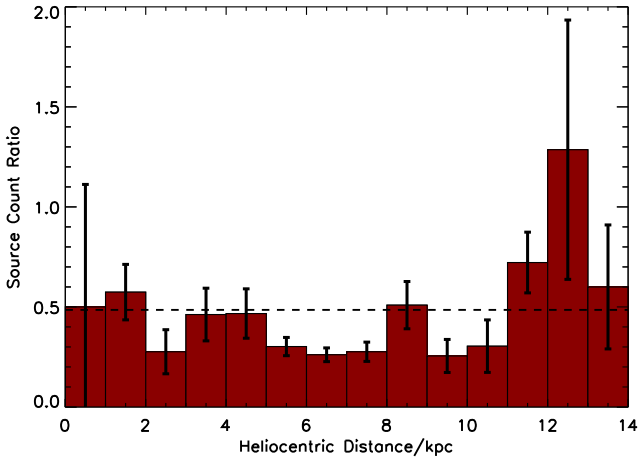

Figure 10. Ratio of the number of YSOs to BGPS clumps as a function of heliocentric distance, with the mean value of 0.49 indicated by the dashed line. The errors are derived using Poissonian statistics.

Perseus arm, the value of $L/M_{\rm clump}$ is less dependent of the inclusion of starless clumps, indicating that there are relatively few of these.

In this scenario, the current gradient of the SFR is relatively flat at radii less than 6.5 kpc, including the Sagittarius arm. In the Scutum–Centaurus tangent, the SFR is set to increase with time and around the Perseus arm, star formation is currently relatively advanced and the production rate of clouds and of clumps within clouds is not keeping pace with the star formation. This picture is consistent with the known patchy nature of star formation in spiral arms and elsewhere (e.g. Urquhart et al. 2014b) which naturally suggests that it is also intermittent in time. It may also require that the time-scale for the IR-traced star formation is longer than that for the production of dense clumps, so that clump production does not keep up, or that the dense clumps are aboriginal cloud features that are not replaced. It is usually assumed that since the time-scales associated with the star-formation stages traced by IR and submm emission are a few $\times 10^5$ years or less (Mottram et al. 2011b; Ginsburg et al. 2012), then these tracers give a snapshot of current star formation, with little or no look-back time.

As shown in Eden et al. (2012, 2013) and in Fig. 8, the distributions of the CFE and SFE of different populations of individual clouds all follow statistically indistinguishable lognormal distributions. Since spiral arms generally have more star formation in them, the spiral-arm populations are larger and sample further into the wings of the $L/M_{\rm clump}$ probability distribution, and so include more very high (and very low) SFE clouds and clumps but, since $L(M)$ for massive, star-forming clumps is linear rather than ZAMS-like (e.g. Urquhart et al. 2014b), the sample average of $L/M_{\rm clump}$ does not depend on sample size and should not vary between arm and interarm populations for that reason. This does not rule out the possibility of some local variance produced by the inclusion of occasional extreme objects, as found in Moore et al. (2012).

A physical explanation as to why $L/M_{\rm clump}$ should be generally enhanced in spiral-arm clumps is elusive. Star formation time-scales may be longer in longer lasting and generally more massive clouds (Dobbs et al. 2011), but there is no independent evidence to support this. Positive feedback (i.e. triggering) in crowded regions might be involved, although models suggest that this is not a significant effect (Dale et al. 2014) and there is no indication that clumps in spiral-arm clouds are physically different from those elsewhere. While a more definitive resolution of this question requires studies of larger samples, results so far contain no strong evidence of significant variations in SFE on kpc scales that cannot be ascribed to the inclusion of extreme objects in the samples and hence no indication that large-scale mechanisms in general, and spiral arms in particular, are important in regulating Galactic star formation. The fact that variations in conditions within individual clouds are much more significant, as outlined in Section 4.4, implicates cloud-scale mechanisms such as the initial conditions of cloud formation, cloud collisions or local feedback as the key factors.

5.2 Potential sources of bias

5.2.1 *Distance dependence of* L/M *and completeness*

One source of potential bias relating to the L/M ratio is the distance. There are three ways in which distance effects could alter the L/M ratio: the nearby clumps have elevated L/M ratios due to a greater detection percentage of YSOs, the most distant clouds having a deficit due to the YSO completeness dropping off before the BGPS completeness or the inverse of this and the lack of BGPS completeness pushing the L/M ratio up.

The detection limits of the YSO-tracing surveys could simultaneously increase the L/M ratios nearby and decrease it at further distances. A larger percentage of IR sources would be observed in nearby clumps and clouds as the lower luminosity sources would have been detected. This effect would work in reverse at larger distances. This effect is not seen in Fig. 10 which shows a flat distribution in the ratio of numbers of YSOs to clumps. The flatness of the distribution indicates that the surveys trace similar distances, with no enhancement or suppression of the ratio at the furthest distances. It is worth noting that any YSOs detected in nearby clumps, but missed at far distances, will be low luminosity and will not add much to $L/M_{\rm clump}$. In the reverse case, undetected clumps at further distances will not be associated with any bright YSOs.

The respective completeness limits of the two surveys could also alter the result. The BGPS has a completeness limit of ∼550 $M_\odot$ at 14 kpc (Rosolowsky et al. 2010), whilst the YSO luminosity is limited by the least sensitive survey, Hi-GAL 70 μm, but has a completeness limit at ∼675 $L_\odot$ at 14 kpc (Elia et al. 2013). These surveys are similarly sensitive out to the furthest distances sampled

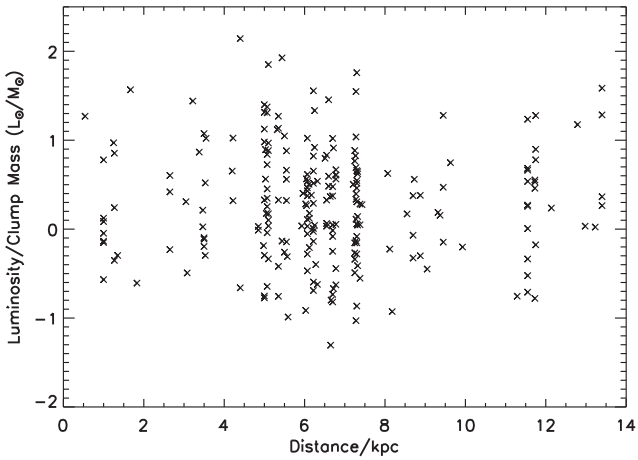

Figure 11. L/M ratio for individual clumps as a function of distance in the $l = 30^\circ$ and 40° regions.

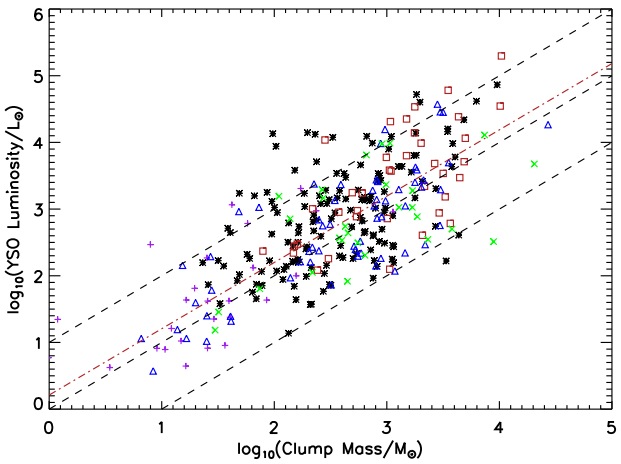

Figure 12. Clump mass–luminosity relationship for the matched YSOs and BGPS clumps. The $l = 30^\circ$ populations of the foreground, tangent and background regions are represented by purple plus symbols, black stars and red squares, respectively, with the $l = 40^\circ$ arm and interarm sources represented by blue triangles and green crosses, respectively. The lower, middle and upper black dashed lines represent the $L/M_{\rm clump} = 0.1$, 1 and 10 $\rm L_\odot/M_\odot$, respectively. The red dot–dashed line represents the fit to the data.

in this study, and the lack of distance bias is shown in Fig. 11, with a flat distribution found.

5.2.2 *Area of Galaxy studied*

The regions sampled in this study are relatively narrow, in terms of the entire Galactic plane. However, it is unlikely that this introduces a significant bias as our results are fully consistent with that of Moore et al. (2012) who found similar increases in $L/M_{\rm cloud}$ over a much greater fraction of the Galaxy.

5.2.3 *Assumed spiral arm model*

For this work, and those of the CFE analysis (Eden et al. 2012, 2013), a four-armed model of the Galaxy is adopted. This model is preferred over contrasting two-arm models, determined from the kinematics of Two Micron All-Sky Survey sources (Francis & Anderson 2012), or three-arm models from the distributions of giant molecular clouds (Solomon et al. 1987).

The four-armed model is preferred due to the vast number of different tracers which outline four arms, from H II regions (e.g. Paladini et al. 2004) to H I distributions (Levine et al. 2006) to combinations of tracers (e.g. Hou et al. 2009). However, the YSO population of the Galaxy is consistent with a four-arm model (Urquhart et al. 2014a), and as we are tracking the YSO population, this is the best choice.

The choice of this model over others would have a bearing on the arm/interarm separation of the sources. It, however, would not have a bearing on the Galactocentric radius distribution. As such it would be clear that on the scale of individual clumps we would still see the large variation as seen in Fig. 8 but the variations on kiloparsec scales would be averaged out.

5.3 Clump mass–luminosity relation

The relationship between clump mass and YSO luminosity is displayed in Fig. 12. There appears to be a correlation, but both quantities have a strong distance dependence. Therefore, to test the correlation, a partial Spearman correlation test, which takes into account the dependence on a common variable (distance in this case), was used. This gave a correlation coefficient of 0.56 with a p-value of $\sim\times\ 10^{-7}$ that this correlation occurred by chance for the sample of 298 BGPS clumps. By selecting a distance-limited sample between 4 and 6 kpc, a correlation coefficient of 0.52 with a p-value of $\sim\times 10^{-5}$ is found; therefore, there is no evidence for any significant systematic distance effect on the observed relationship.

Interpretation of the L–$M_{\rm clump}$ relation is difficult if the L and $M_{\rm clump}$ are derived from the same data (e.g. Veneziani et al. 2013), which is particularly the case if $L = L_{\rm bol}$, hence the use of $L_{\rm IR}$ instead of $L_{\rm bol}$ to attempt to remove the dependence of both quantities on the submm component of the SED. The linear log–log fit of $L_{\rm IR}$ with $L_{\rm bol}$ in Fig. 3 is the result of YSO SEDs being essentially greybody spectra and that the sources are selected in the same way i.e. by waveband, with small variations, such as the temperature differences reflected in the differing colours of the sources and the independence of $L_{\rm IR}$ and $L_{\rm bol}$ causing the scatter.

The slope of the linear log–log fit found for this distribution is 0.99 ± 0.04, which is slightly shallower than that of Molinari et al. (2008), but is consistent with that of Urquhart et al. (2014b) who found slopes of 1.27 ± 0.08 and 1.09 ± 0.13, respectively. The slope of the linear fit to the distance-selected sample mentioned above is 0.89 ± 0.18.

Further to this correlation, the L–$M_{\rm clump}$ relation can be used to derive the evolutionary state of the YSO as it approaches the main sequence (Molinari et al. 2008; Giannetti et al. 2013). Molinari et al. (2008) highlight two phases in this evolution in the L–$M_{\rm clump}$ plane: the main accretion and envelope clean-up phases, using the accelerating accretion rates as postulated by (McKee & Tan 2003). Once the clump is formed, the gradient of the locus in L–$M_{\rm clump}$ space will begin at $L_{\rm IR} = 0$, as there would be no YSOs present, and so $L_{\rm IR}$ will be zero. The gradient will be 1 if $L = L_{\rm bol}$ and the temperature is constant with L and M. As YSOs form, the luminosity will be made up of two components, the accretion luminosity and the luminosity of the source. If the accretion luminosity, $L_{\rm acc}$, dominates the YSO luminosity, then this implies a high accretion rate and/or a very early stage prior to fusion. The luminosity thus increases at near-constant mass on a vertical track in L–$M_{\rm clump}$ space. Once the accretion finishes, the envelope begins to be dispersed. The YSOs find themselves clustering at $L/M_{\rm clump} = 1\ \rm L_\odot/M_\odot$ as sources

spend a relatively long time in the region where accretion is ending and envelope clearance has not yet commenced. Both the accretion rate and envelope clean-up rate increase with time with the accretion rate increasing as the mass of the protostar increases (McKee & Tan 2003; Davies et al. 2011). The clean-up phase starts slowly as it takes some time for the embedded star to disrupt the clump from which it formed. The final luminosity is dependent on the initial clump mass, and as a result a linear log–log distribution is found, especially as the accretion luminosity is proportional to the stellar mass (McKee & Tan 2003). This dependence, $L \propto M_*^{0.95}$, implies that the accretion luminosity is proportional to the initial clump mass due to the relationship between stellar mass and clump mass (McKee & Tan 2003).

Once the clearing is finished, the YSOs move to the left in L–$M_{\rm clump}$ space, which is a very quick phase, hence why no very-high-luminosity, low-mass sources are found. By selecting sources in the mid-IR, we may be filtering out the envelope-clearing and pre-stellar sources. This begins the evolution from the slope of unity towards the mass–luminosity relation of either main-sequence stars ($L \propto M^{3.5}$) or clusters ($L \propto M^2$).

The distribution also implies that there is a constant $L/M_{\rm clump}$ ratio acting along the spectrum of clump masses. It, however, requires that the instantaneous SFE, i.e. the mass of stars formed from a particular mass of dense gas, acting on each clump varies as a function of clump mass (Urquhart et al. 2014b). Urquhart et al. (2014b) suggest that the SFE is lower for the high-mass and high-luminosity sources in which the high-mass members of a cluster form first. The disparity between the observed and cluster relationships is seen by both Sridharan et al. (2002) and Urquhart et al. (2014b). Both of those studies show that the lower mass clumps are over luminous, whilst the higher mass clumps are not as luminous as one would expect if each source was expected to be the site of cluster formation and a standard IMF was sampled at a constant SFE. However, the observed dependence is consistent with the relationship between accretion luminosity and stellar mass ($L \propto M^{0.95}$) and that of accretion luminosity and final stellar mass ($L \propto M^{1.20}$; McKee & Tan 2003). This implies that these sources are either still accreting or have just reached the final stellar mass.

6 SUMMARY AND CONCLUSIONS

We have combined a series of surveys tracing IR YSOs with the BGPS sample of star-forming clumps within two slices of the Galactic plane, in order to investigate how the SFE, measured as the ratio of IR luminosity to clump mass, varies with Galactic environment. The two slices of the Galactic plane, centred at Galactic longitudes of $l = 30^\circ$ and 40°, cover spiral-arm regions, interarm regions and the end of the Galactic Long Bar, which contains the star-forming region, W43.

As a result of positionally matching IR sources to BGPS clumps using the sample subsets from Eden et al. (2012, 2013), we find a total of 348 candidate YSOs associated with 298 distinct clumps, which accounts for 29 per cent of the BGPS sources found in the two regions. The distances, and Galactic environments, of the BGPS sources and the luminosities of the associated YSO sources were taken from the derived distances in Eden et al. (2012, 2013).

In order to obtain a YSO luminosity independent of the clump mass, we used only wavelengths shorter than 70 μm to calculate $L_{\rm IR}$ and the 1.1-mm flux density for $M_{\rm clump}$. The method for calculating the luminosities was to use a trapezium rules integration in that wavelength range as the use of the bolometric luminosity from the Robitaille SED fitting tools (Robitaille et al. 2006, 2007) included the contribution from the envelope in which the YSO is embedded, i.e. the clump, and an independent measure of the YSO luminosity from the clump component was required. The absolute luminosities found using both methods were found to be different but the relative differences were consistent across all distances and environments.

We compared the ratio of IR luminosity, $L_{\rm IR}$, to the clump mass, $M_{\rm clump}$, as a function of Galactic environment, and the properties of clumps hosting a candidate YSO and our main findings are as follows:

(i) In the $l = 30^\circ$ region, the $L_{\rm IR}/M_{\rm clump}$ ratio is larger in the background spiral arms by a factor of $\sim$2.5 compared to the other $l = 30^\circ$ populations, including the W43 star-forming region. This is consistent with the results of Moore et al. (2012) who found that the Sagittarius and Perseus arms had a higher $L_{\rm IR}/M_{\rm cloud}$ ratio than the Scutum–Centaurus arm. This may imply that the future SFR of W43 will be higher than the current observed rate, as suggested by Nguyen Luong et al. (2011).

(ii) The luminosity distributions for the Scutum–Centaurus tangent region and a combined spiral-arm sample, made up of Sagittarius and Perseus arm sources, are consistent with each other. This supports the $M_{\rm clump}/M_{\rm cloud}$ results of Eden et al. (2012) that the mass function at the end of the bar is not significantly different from any other spiral arm in the Galaxy and that there is no enhancement in the SFR per clump mass due to the interaction of the bar with spiral arms.

(iii) The observed distribution of $L_{\rm IR}/M_{\rm clump}$ ratios for all clumps is consistent with a lognormal probability function, implying that those with extreme values, both low and high, are the result of the same combination of random processes and do not indicate the presence of fundamentally different conditions.

(iv) Assuming a single star forming from each YSO, the average absolute SFE, ratio of stellar mass to clump mass, was found to be 1.9 ± 0.2 per cent.

(v) The ranges of L/M found for the individual clumps, molecular clouds and spiral arms were found to be 0.04 ± 0.01–140 ± 22, 0.02 ± 0.01–68 ± 13 and 1.00 ± 0.02–2.9 ± 0.2 $L_\odot/M_\odot$, respectively.

(vi) Combining these results with others investigating the role of spiral arms on the star formation process, it is found that, on kiloparsec scales, there is little evidence of significant variations in SFE that can be attributed to the action of the arms on the ISM. Differences in average $L_{\rm IR}/M_{\rm clump}$ found in spiral-arm sources may be due to gradients in the SFR or local variance in the limited samples. The most significant variations in SFE are found to be on the scales of individual molecular clouds and clumps.

(vii) There is a linear relationship between the $L_{\rm IR}$ and $M_{\rm clump}$ with a best-fitting power-law exponent of 0.99 ± 0.04, which is consistent with that of Molinari et al. (2008) and Urquhart et al. (2014b).

ACKNOWLEDGEMENTS

The authors wish to thank the anonymous referee for comments that have improved the quality of the paper. This work is based in part on observations made with the *Spitzer Space Telescope*, which is operated by the Jet Propulsion Laboratory, California Institute of Technology under a contract with NASA. This publication makes use of data products from the *WISE*, which is a joint project of the University of California, Los Angeles and the Jet Propulsion Laboratory/California Institute of Technology, funded by the National Aeronautics and Space Administration. DJE wishes to acknowledge

an STFC PhD studentship for this work. This research has made use of NASA's Astrophysics Data System.

REFERENCES

Aguirre J. E. et al., 2011, ApJS, 192, 4
Benjamin R. A. et al., 2003, PASP, 115, 953
Churchwell E. et al., 2009, PASP, 121, 213
Compiègne M., Flagey N., Noriega-Crespo A., Martin P. G., Bernard J.-P., Paladini R., Molinari S., 2010, ApJ, 724, L44
Csengeri T. et al., 2014, A&A, 565, A75
Dale J. E., Ngoumou J., Ercolano B., Bonnell I. A., 2014, MNRAS, 442, 694
Davies B., Hoare M. G., Lumsden S. L., Hosokawa T., Oudmaijer R. D., Urquhart J. S., Mottram J. C., Stead J., 2011, MNRAS, 416, 972
Dobbs C. L., Pringle J. E., 2013, MNRAS, 432, 653
Dobbs C. L., Bonnell I. A., Pringle J. E., 2006, MNRAS, 371, 1663
Dobbs C. L., Burkert A., Pringle J. E., 2011, MNRAS, 417, 1318
Dunham M. K., Rosolowsky E., Evans II N. J., Cyganowski C., Urquhart J. S., 2011, ApJ, 741, 110
Eden D. J., Moore T. J. T., Plume R., Morgan L. K., 2012, MNRAS, 422, 3178
Eden D. J., Moore T. J. T., Morgan L. K., Thompson M. A., Urquhart J. S., 2013, MNRAS, 431, 1587
Elia D. et al., 2013, ApJ, 772, 45
Elmegreen B. G., 2006, ApJ, 648, 572
Elmegreen B. G., Elmegreen D. M., 1986, ApJ, 311, 554
Fazio G. G. et al., 2004, ApJS, 154, 10
Foyle K., Rix H.-W., Walter F., Leroy A. K., 2010, ApJ, 725, 534
Francis C., Anderson E., 2012, MNRAS, 422, 1283
Georgelin Y. M., Georgelin Y. P., 1976, A&A, 49, 57
Giannetti A. et al., 2013, A&A, 556, A16
Giannini T. et al., 2012, A&A, 539, A156
Ginsburg A., Bressert E., Bally J., Battersby C., 2012, ApJ, 758, L29
Griffin M. et al., 2008, Proc. SPIE, 7010, 701006
Heyer M. H., Terebey S., 1998, ApJ, 502, 265
Hou L. G., Han J. L., Shi W. B., 2009, A&A, 499, 473
Jackson J. M. et al., 2006, ApJS, 163, 145
Johnston K. G., Shepherd D. S., Aguirre J. E., Dunham M. K., Rosolowsky E., Wood K., 2009, ApJ, 707, 283
Krumholz M. R., Cunningham A. J., Klein R. I., McKee C. F., 2010, ApJ, 713, 1120
Lada C. J., Lada E. A., 2003, ARA&A, 41, 57
Levine E. S., Blitz L., Heiles C., 2006, Science, 312, 1773
Lumsden S. L., Hoare M. G., Urquhart J. S., Oudmaijer R. D., Davies B., Mottram J. C., Cooper H. D. B., Moore T. J. T., 2013, ApJS, 208, 11
McKee C. F., Tan J. C., 2003, ApJ, 585, 850
Meynet G., Maeder A., 2003, A&A, 404, 975
Molinari S., Pezzuto S., Cesaroni R., Brand J., Faustini F., Testi L., 2008, A&A, 481, 345
Molinari S. et al., 2010a, PASP, 122, 314
Molinari S. et al., 2010b, A&A, 518, L100
Molinari S., Schisano E., Faustini F., Pestalozzi M., di Giorgio A. M., Liu S., 2011, A&A, 530, A133
Moore T. J. T., Urquhart J. S., Morgan L. K., Thompson M. A., 2012, MNRAS, 426, 701
Motte F., Schilke P., Lis D. C., 2003, ApJ, 582, 277
Mottram J. C. et al., 2011a, A&A, 525, A149
Mottram J. C. et al., 2011b, ApJ, 730, L33
Nguyen Luong Q. et al., 2011, A&A, 529, A41
Paladini R., Davies R. D., De Zotti G., 2004, MNRAS, 347, 237
Poglitsch A. et al., 2008, Proc. SPIE, 7010, 701005
Price S. D., Egan M. P., Carey S. J., Mizuno D. R., Kuchar T. A., 2001, AJ, 121, 2819
Roberts W. W., 1969, ApJ, 158, 123
Robitaille T. P., Whitney B. A., Indebetouw R., Wood K., Denzmore P., 2006, ApJS, 167, 256
Robitaille T. P., Whitney B. A., Indebetouw R., Wood K., 2007, ApJS, 169, 328
Roman-Duval J., Jackson J. M., Heyer M., Johnson A., Rathborne J., Shah R., Simon R., 2009, ApJ, 699, 1153
Rosolowsky E. et al., 2010, ApJS, 188, 123
Smith M. D., 2014, MNRAS, 438, 1051
Solomon P. M., Rivolo A. R., Barrett J., Yahil A., 1987, ApJ, 319, 730
Sridharan T. K., Beuther H., Schilke P., Menten K. M., Wyrowski F., 2002, ApJ, 566, 931
Urquhart J. S. et al., 2013a, MNRAS, 431, 1752
Urquhart J. S. et al., 2013b, MNRAS, 435, 400
Urquhart J. S., Figura C. C., Moore T. J. T., Hoare M. G., Lumsden S. L., Mottram J. C., Thompson M. A., Oudmaijer R. D., 2014a, MNRAS, 437, 1791
Urquhart J. S. et al., 2014b, MNRAS, 443, 1555
Vallee J. P., 1995, ApJ, 454, 119
Veneziani M. et al., 2013, A&A, 549, A130
Vogel S. N., Kulkarni S. R., Scoville N. Z., 1988, Nature, 334, 402
Weidner C., Kroupa P., 2006, MNRAS, 365, 1333
Weidner C., Kroupa P., Bonnell I. A. D., 2010, MNRAS, 401, 275
Wright E. L. et al., 2010, AJ, 140, 1868

This paper has been typeset from a TEX/LATEX file prepared by the author.